energies

MDPI

Article

Impact of Leading-Edge Tubercles on Airfoil Aerodynamic Performance and Flow Patterns at Different Reynolds Numbers

Dian Wang [1], Chang Cai [2,3,*], Rongyu Zha [1], Chaoyi Peng [4], Xuebin Feng [4], Pengcheng Liang [4], Keqilao Meng [5], Jianyu Kou [6], Takao Maeda [7] and Qing'an Li [2,3,8,*]

1 CRRC Qi Hang New Energy Technology Co., Ltd., Beijing 100192, China
2 National Energy Wind Turbine Blade R&D Center, Institute of Engineering Thermophysics, Chinese Academy of Sciences, Beijing 100190, China
3 The Key Laboratory of Wind Energy Utilization of Chinese Academy of Sciences, Beijing 100190, China
4 Zhuzhou Times New Materials Technology Co., Ltd., Zhuzhou 412007, China
5 School of Energy and Power Engineering, Inner Mongolia University of Technology, Hohhot 010051, China
6 Inner Mongolia Energy Group Co., Ltd., Hohhot 010051, China
7 Division of Mechanical Engineering, Mie University, Tsu 514-8507, Japan
8 University of Chinese Academy of Sciences, Beijing 100049, China
* Correspondence: caichang@iet.cn (C.C.); liqingan@iet.cn (Q.L.)

Abstract: In recent years, leading-edge tubercles have gained significant attention as an innovative biomimetic flow control technique. This paper explores their impact on the aerodynamic performance and flow patterns of an airfoil through wind tunnel experiments, utilizing force measurements and tuft visualization at Reynolds numbers between 2.7×10^5 and 6.3×10^5. The baseline airfoil exhibits a hysteresis loop near the stall angle, with sharp changes in lift coefficient during variations in the angle of attack (AOA). In contrast, the airfoil with leading-edge tubercles demonstrates a smoother stall process and enhanced post-stall performance, though its pre-stall performance is slightly reduced. The study identifies four distinct flow regimes on the modified airfoil, corresponding to different segments of the lift coefficient curve. As the AOA increases, the flow transitions through stages of full attachment, trailing-edge separation, and local leading-edge separation across some or all valley sections. Additionally, the study suggests that normalizing aerodynamic performance based on the valley section chord length is more effective, supporting the idea that leading-edge tubercles function like a series of delta wings in front of a straight-leading-edge wing. These insights provide valuable guidance for the design of blades with leading-edge tubercles in applications such as wind and tidal turbines.

Keywords: leading-edge tubercles; flow control; airfoil; aerodynamic performance; flow visualization

check for updates

Citation: Wang, D.; Cai, C.; Zha, R.; Peng, C.; Feng, X.; Liang, P.; Meng, K.; Kou, J.; Maeda, T.; Li, Q. Impact of Leading-Edge Tubercles on Airfoil Aerodynamic Performance and Flow Patterns at Different Reynolds Numbers. *Energies* **2024**, *17*, 5518. https://doi.org/10.3390/en17215518

Academic Editor: Andrey A. Kurkin

Received: 2 October 2024
Revised: 20 October 2024
Accepted: 22 October 2024
Published: 4 November 2024

Copyright: © 2024 by the authors. Licensee MDPI, Basel, Switzerland. This article is an open access article distributed under the terms and conditions of the Creative Commons Attribution (CC BY) license (https://creativecommons.org/licenses/by/4.0/).

1. Introduction

In recent years, leading-edge tubercles have attracted significant attention as an innovative biomimetic flow control technique [1–5]. This concept is inspired by humpback whales, known for their exceptional maneuverability despite their large, rigid bodies [3]. Studies have shown that the tubercles along the leading edges of their flippers enhance hydrodynamic performance at high angles of attack (AOAs), improving agility [6]. Due to its broad effectiveness, this flow control method holds great potential for various applications, such as wind turbines [7–10], tidal turbines [11–14], and propellers [15–17]. However, many of these applications are still in the conceptual or experimental stages, and substantial improvements in the overall performance of hydrodynamic and aerodynamic systems have yet to be realized. To fully leverage the potential of this technique, a deeper understanding of the flow structures generated by leading-edge tubercles and the mechanisms underlying their flow control capabilities is essential.

Various methods have been employed to modify the leading edge of an airfoil by mimicking the humpback whale flipper. In most studies, the leading edge is designed as a sinusoidal curve, with the average chord length matching that of the baseline airfoil with a straight leading edge [18–21]. In other research, sinusoidal or spherical tubercles are extruded from the baseline airfoil, resulting in an average chord length larger than the baseline [22–25]. Additionally, in a study conducted by Stalnov et al. [26], sinusoidal leading edges were directly cut into the main body of the wing. Despite differences in these modification techniques, all modified airfoils show similar performance characteristics, particularly improved post-stall behavior compared to the baseline airfoil [2]. However, their pre-stall performance generally declines, with lower lift coefficients and higher drag coefficients to varying degrees [2]. It is important to note that the methods for calculating lift and drag coefficients differ across these studies. The first type of leading-edge modification typically uses the averaged chord length and planform area of the modified airfoil as the characteristic length and area [17–20], whereas the second type often uses the baseline airfoil's chord length and planform area, which may differ from the modified airfoil's averaged values [22–25]. In the research of Stalnov et al. [26], the lift coefficient was normalized using the baseline chord, mean chord, and valley chord, respectively. They found that when the lift coefficient is defined based on the valley chord, uniformity in the lift curve slope is achieved, though further verification of this approach is necessary. Currently, there is no consensus on the most appropriate method for scaling the aerodynamic performance of an airfoil modified with leading-edge tubercles.

Previous studies have identified various flow characteristics induced by leading-edge tubercles. Johari et al. [18], using tuft visualization, found that flow separation occurs earlier in the valleys between tubercles and is delayed at the peaks. The stable attached flow over the peaks is believed to enhance post-stall performance. This phenomenon has also been observed and confirmed through other techniques, such as oil flow visualization [27], particle image velocimetry (PIV) [20,28], and numerical simulations [29–31]. Additionally, it is widely accepted that the counter-rotating streamwise vortices generated by the tubercles play a critical role in flow control. Evidence for this has been provided by dye visualization experiments [32], hydrogen-bubble visualization [19], PIV experiments [28,33], and computational fluid dynamics using various numerical methods [24,33,34]. Although leading-edge tubercles are typically designed with periodic sinusoidal distributions, recent studies have shown that the flow around each tubercle may not be spatially periodic. This phenomenon was first observed by Custodio [32] in dye visualization experiments and has since been verified by multiple numerical studies [24,35]. One factor that may contribute to this biperiodic flow pattern is the number of protuberances on the modified airfoil. More complex aperiodic flow patterns have been reported in airfoils with more than four protuberances [24,36–38].

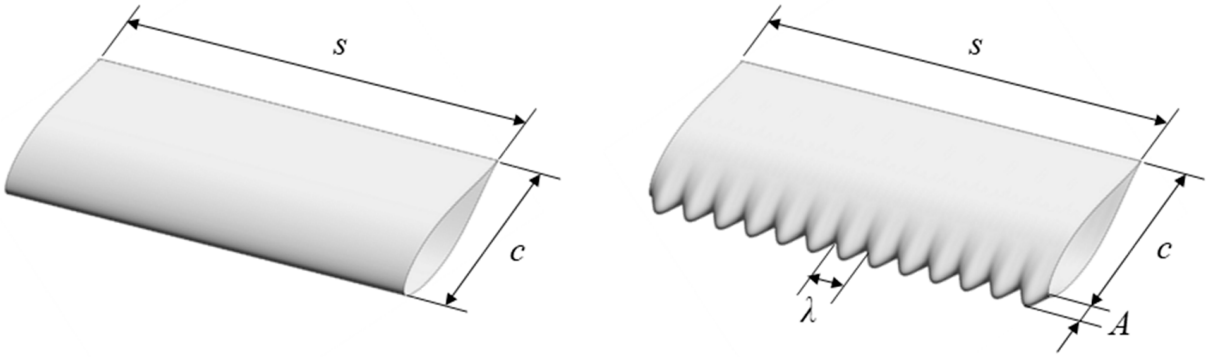
Several hypotheses have been proposed to explain the flow control mechanism of leading-edge tubercles from different perspectives. The most widely accepted theory is that leading-edge tubercles function similarly to vortex generators [6,19,28]. By generating streamwise vortices, tubercles enhance the exchange of momentum between the freestream and the boundary layer, thereby delaying boundary layer separation. More recently, Seyhan et al. [39] suggested that tubercles function more like stall strips rather than vortex generators. Another hypothesis posits that the primary role of the streamwise vortices is to induce a downwash velocity around the peaks, reducing the sectional effective AOA and delaying local stall [40,41]. A similar view compares tubercles to a series of small delta wings positioned ahead of the leading edge, which improve airfoil performance through vortex lift [32,42]. Another important hypothesis is the compartmentalization effect. Originally proposed by Watts and Fish [43], this theory suggests that tubercles act similarly to wing fences, preventing spanwise flow. This idea is supported by a numerical study by Pedro and Kobayashi [44] on a three-dimensional flipper model, as well as by experimental and numerical studies by Cai et al. on a modified airfoil with a single or multiple leading-edge tubercle [45,46].

Based on the literature review, several underlying issues related to leading-edge tubercles remain unresolved: (1) The relationship between aerodynamic performance and flow patterns is unclear. (2) There is no consensus on the appropriate scaling method for aerodynamic performance. (3) The flow control mechanism is not fully understood. To address these issues, wind tunnel experiments, including force measurements and tuft visualization, were conducted to investigate the relationship between aerodynamic performance and flow patterns on a modified airfoil with leading-edge tubercles. Different flow regimes were identified and defined based on the key characteristics of the lift coefficient curve and the associated flow patterns, with a discussion on the effects of Reynolds numbers. Building on these findings, we explore both the scaling method for aerodynamic performance and the underlying flow control mechanisms.

2. Test Objects and Method

2.1. Test Airfoils

The experimental airfoil models are shown in Figure 1. The baseline airfoil selected was the NACA 63_4-021, which has a profile resembling the cross-section of humpback whale flippers [3]. It features a chord length (c) of 200 mm and a span (s) of 650 mm. In comparison to the baseline, the modified airfoil includes extruded protuberances along the leading edge. These protuberances follow a cosine curve with 13 periods, a wavelength (λ) of 50 mm, and a peak-to-valley amplitude (A) of 20 mm. At the bottoms of the protuberances, the local airfoil profiles match that of the baseline airfoil. Consequently, the average chord length of the modified airfoil is 210 mm, which is 5% larger than that of the baseline.



(**a**) Baseline (**b**) Modified

Figure 1. Test airfoils.

2.2. Test Rig

The experiments were conducted in a Göttingen-type circular wind tunnel at the Fluid Engineering Laboratory of Mie University in Japan. The wind tunnel features a 650 mm × 650 mm square test section, with a freestream velocity range of 0 to 52 m/s. For a detailed description of the wind tunnel, refer to Refs. [23,24]. The experimental setup, including the test airfoil and associated equipment, is illustrated in Figure 2. A Pitot tube, located at the wind tunnel nozzle outlet, was used to monitor the freestream velocity. A removable turbulence grid was positioned between the Pitot tube and the test section to control the turbulence intensity. The test airfoil was mounted horizontally, with its ends connected to two rotary disks on the side walls of the test section. Two six-component force transducers (LFM-A Compact) were installed outside the walls to measure forces and moments. The entire support system was linked to an AC servomotor (Yaskawa Corp., Kitakyushu, Japan; SGMGH-04A1AH761), allowing for precise adjustment of the angle of attack via computer programming. Two Cartesian coordinate systems are used in this study, as shown in Figure 2. The x, y, and z axes represent the inflow, vertical, and spanwise directions, respectively, while the X, Y, and Z axes correspond to the coordinate system of

the force transducers. The origins of both systems are located at the spanwise center of the airfoil, along the pitching axis, positioned at 0.6*c* from the trailing edge.

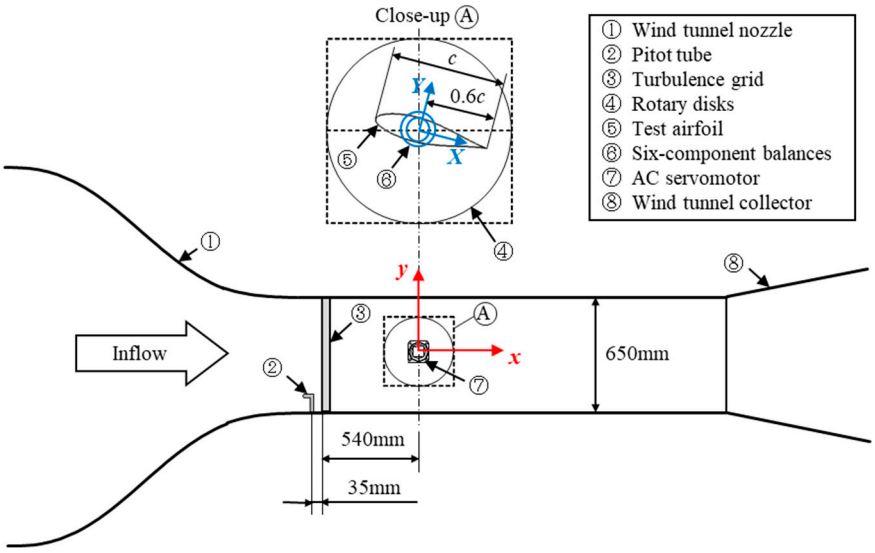


Figure 2. Schematic of the test rig.

2.3. Force Measurement

In this study, the AOA range for force measurements was set between −6° and 30°. The balance system used for force measurement operated at a frequency of 1000 Hz. For each test AOA, the working condition was stabilized for 10 s, after which the balance data were recorded over the next 10 s to calculate the time-averaged forces. The self-weight of the test airfoil and support system, previously measured under zero wind speed conditions for each AOA, was subtracted from the recorded forces. Since the balances rotated along with the airfoil as the AOA changed, an angular transformation was applied to convert the measured forces into aerodynamic forces in the inflow coordinate system:

$$L = F_Y cos\alpha - F_X sin\alpha \tag{1}$$

$$D = F_X cos\alpha + F_Y sin\alpha \tag{2}$$

where L and D represent the aerodynamic lift and drag forces acting on the airfoil, F_X and F_Y are the forces measured in the balance coordinate system, and α is the AOA. The dimensionless lift and drag coefficients were then calculated using the following equations:

$$C_L = \frac{L}{0.5\rho V_\infty^2 A} \tag{3}$$

$$C_D = \frac{D}{0.5\rho V_\infty^2 A} \tag{4}$$

where ρ is the air density, V_∞ is the freestream velocity, and A is the planform area of the baseline airfoil. It is important to note that the chord length of the baseline airfoil was used to normalize the aerodynamic coefficients for both the baseline and modified airfoils, even though the mean chord length of the modified airfoil is 5% larger. This decision follows the recommendation of Stalnov et al. [26], who suggested that the chord length at the valley section of a wavy airfoil with leading-edge tubercles is more appropriate for normalizing aerodynamic coefficients.

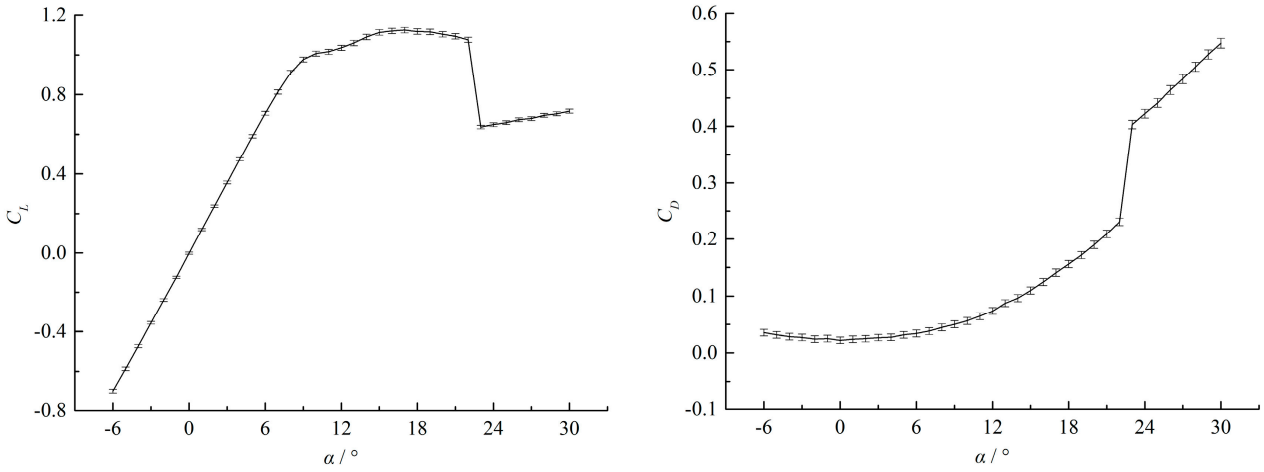
The method proposed by Pope and Ray [47] was applied to correct for the effects of solid and wake blockages caused by wall interference. Additionally, the error bars for the

lift and drag coefficients were derived using the error propagation techniques described in AGARD-AR-304 [48]:

$$\sigma_{C_L} = \sqrt{\left(\frac{\partial C_L}{\partial L}\right)^2 \sigma_L^2 + \left(\frac{\partial C_L}{\partial V_\infty}\right)^2 \sigma_{V_\infty}^2 + \left(\frac{\partial C_L}{\partial \rho}\right)^2 \sigma_\rho^2 + \left(\frac{\partial C_L}{\partial A}\right)^2 \sigma_A^2} \quad (5)$$

$$\sigma_{C_D} = \sqrt{\left(\frac{\partial C_D}{\partial D}\right)^2 \sigma_L^2 + \left(\frac{\partial C_D}{\partial V_\infty}\right)^2 \sigma_{V_\infty}^2 + \left(\frac{\partial C_D}{\partial \rho}\right)^2 \sigma_\rho^2 + \left(\frac{\partial C_D}{\partial A}\right)^2 \sigma_A^2} \quad (6)$$

Among them, the uncertainties in the lift and drag forces were calculated according to Equations (1) and (2) and the error propagation formula, where the balance test values F_X and F_Y have an uncertainty of ± 0.5 N. The uncertainty in the AOA from the expected value is approximately $\pm 0.1°$. The freestream wind velocity uncertainty is $\pm 0.5\%$ of the expected velocity. The machining process introduces a dimensional error of ± 0.2 mm in the chord and span lengths of the airfoils, and the uncertainty in the planform area was further calculated. Over the course of a single test, the maximum air temperature difference was about 3 °C, leading to an estimated air density uncertainty of ± 0.006 kg/m^3. The final lift and drag coefficient curves with error bars of the baseline airfoil at the Reynolds number of 4.5×10^5 are shown in Figure 3.



(**a**) Lift coefficient (**b**) Drag coefficient

Figure 3. Lift and drag coefficients of the baseline airfoil with error bar (Re = 4.5×10^5).

2.4. Tuft Visualization

To observe the flow separation on the suction surface of the test airfoils, a tuft visualization experiment was conducted independently of the force measurements. The tufts were made of embroidery silk, and their arrangement and positioning are shown in Figure 4. Each tuft, 15 mm in length, was spaced 25 mm apart spanwise and 15 mm apart streamwise on the suction surface. The first row of tufts on the baseline airfoil was positioned 10 mm from the leading edge. In total, 13 rows and 17 columns of tufts were placed on the baseline airfoil, covering approximately two-thirds of the surface area around the span center. For the modified airfoil with extended leading-edge tubercles, an additional tuft was placed at each peak section.

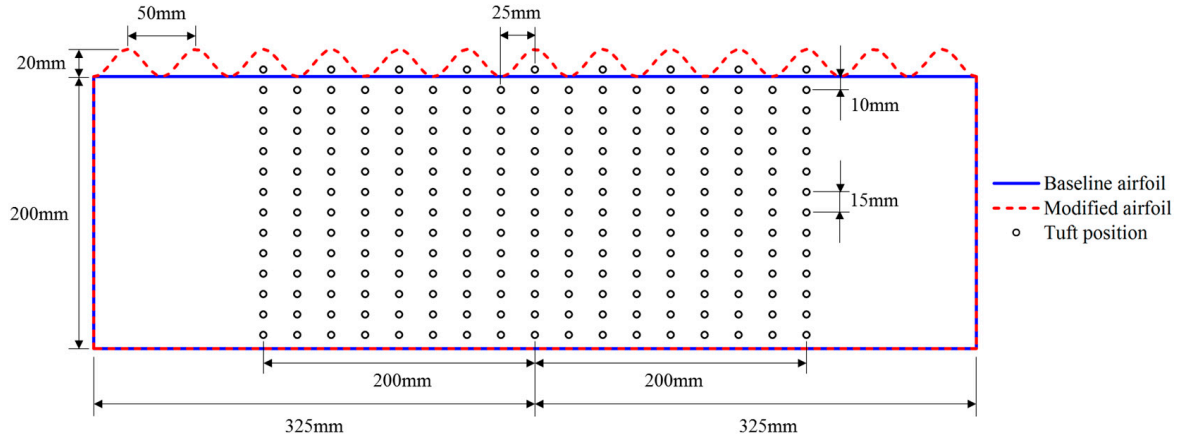
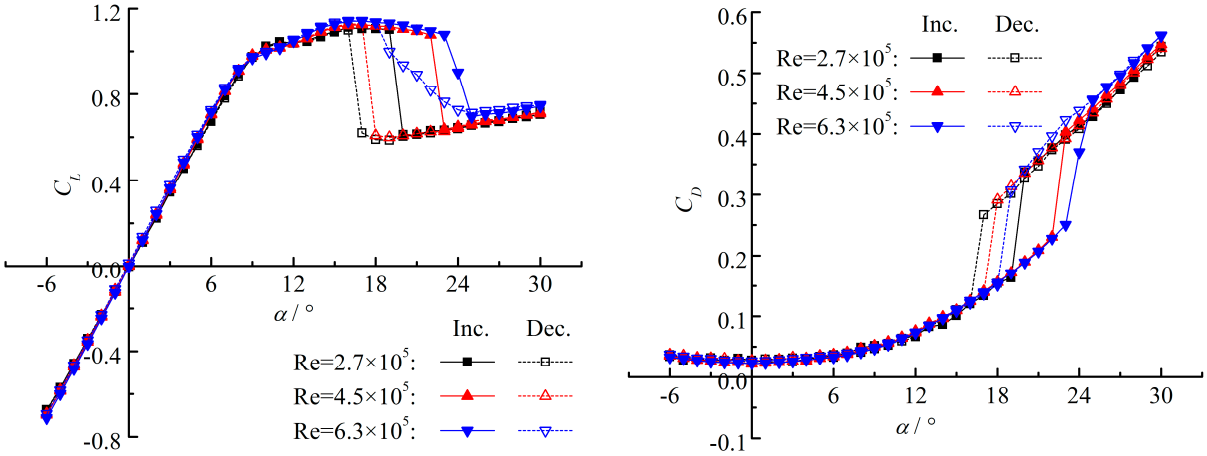


Figure 4. The pasting position of tufts on the suction surface of the test airfoils.

3. Results and Discussion

3.1. Aerodynamic Performance

The aerodynamic performance of the baseline airfoil is illustrated in Figure 5 for Reynolds numbers ranging from 2.7×10^5 to 6.3×10^5. To account for potential hysteresis effects, both increasing and decreasing AOA cases were examined. The lift and drag coefficients of the baseline airfoil exhibit typical characteristics of combined trailing-edge and leading-edge stall, as defined by Mccullough et al. [49]. For all tested Reynolds numbers, the lift coefficient increases linearly with AOA up to approximately $\alpha \approx 9°$. Beyond this point, the increase rate of the lift coefficient slows, while the drag coefficient rises rapidly, indicating the onset and progression of trailing-edge separation. A semi-rounded peak in the lift curve is observed around $\alpha = 17°$ for all Reynolds numbers. As the AOA continues to increase past the stall angle, the lift coefficient experiences a significant drop, accompanied by a marked increase in drag. The stall angle increases from 20° to 25° as the Reynolds number increases from 2.7×10^5 to 6.3×10^5. The post-stall lift coefficient remains relatively low, around 0.7, and increases at a slow rate with further increases in AOA.



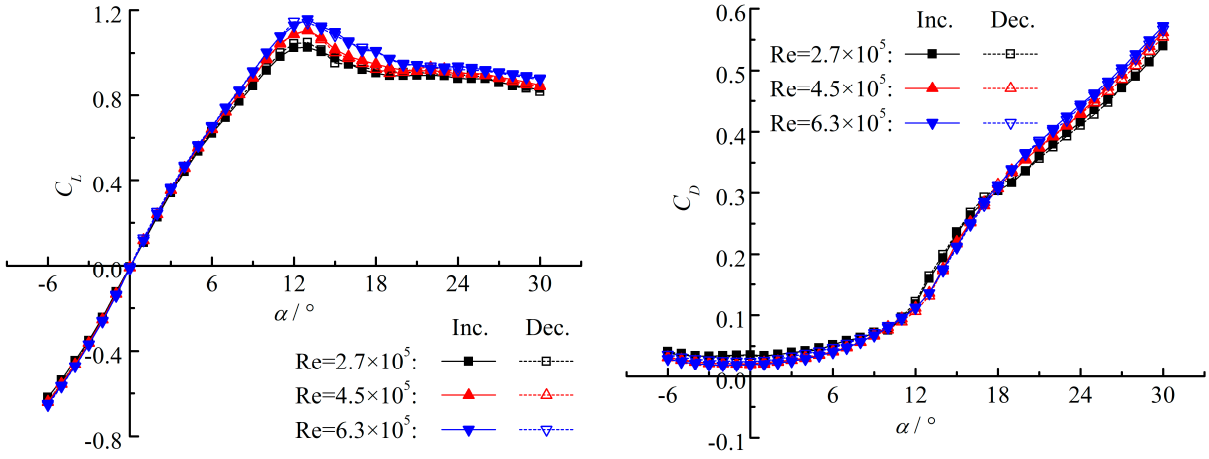
(**a**) Lift coefficient (**b**) Drag coefficient

Figure 5. Effect of Reynolds number on the aerodynamic performance of the baseline airfoil.

For the AOA decreasing case, hysteresis effects are pronounced. The lift coefficient remains at the stalled level and does not return to pre-stall values until the AOA decreases to a lower critical value than the stall angle. The restoration angles vary from 16° to 18° with increasing Reynolds numbers. Notably, at the highest Reynolds number of 6.3×10^5,

the lift coefficient restoration is relatively gradual, spanning from 24° to 18°, indicating increased instability under these conditions.

The aerodynamic performance of the modified airfoil across various Reynolds numbers is shown in Figure 6. At a low AOA of around 6°, the lift coefficient increases but deviates slightly from a linear trend. The maximum lift coefficient occurs at approximately 13°, followed by a gradual decline between 13° and 19°. During this range, the drag coefficient increases at a relatively high rate. At higher AOAs, the lift coefficient stabilizes around 0.9, exceeding the post-stall lift coefficient of the baseline airfoil. The overall trend in lift coefficient remains consistent across different Reynolds numbers, with the curve shifting slightly higher between 6° and 30° as the Reynolds number increases. The modified airfoil shows little hysteresis; the lift and drag coefficients during decreasing AOAs closely match those during increasing AOAs for all Reynolds numbers tested. Overall, the aerodynamic performance of the modified airfoil demonstrates less sensitivity to the Reynolds number compared to the baseline airfoil.



(**a**) Lift coefficient (**b**) Drag coefficient

Figure 6. Effect of Reynolds number on the aerodynamic performance of the modified airfoil.

Figure 7 compares the aerodynamic performance of the baseline and modified airfoils with the theoretical lift curve. The lift–curve slope of the baseline airfoil closely matches the ideal lift curve. As the Reynolds number increases, the lift–curve slope increases slightly, and the AOA's deviation from the linear segment decreases. Comparing the lift curve of the modified airfoil with the baseline, the curves are nearly identical at AOAs below 45. At higher AOAs, the lift coefficient begins to increase linearly but at a lower rate, reaching its maximum at around 12° to 13°. In this range, the lift coefficient of the modified airfoil is lower than that of the baseline airfoil at Re = 2.7 × 10^5. However, as the Reynolds number increases, the lift coefficient of the modified airfoil slightly surpasses that of the baseline airfoil at around 12°. The drag coefficient of the modified airfoil increases slightly compared to the baseline airfoil across all Reynolds numbers. As the AOA increases further, the lift coefficient of the modified airfoil starts to decrease, with the drag coefficient significantly higher than the baseline airfoil between 12° and 18°. At even larger AOAs, the lift coefficient of the modified airfoil remains nearly constant and is higher than that of the baseline airfoil in deep stall conditions, while the drag coefficient follows a similar trend to the baseline airfoil in deep stall. The comparison of lift-to-drag ratios reveals that the modified airfoil has a lower maximum lift-to-drag ratio than the baseline airfoil, primarily due to an increase in the drag coefficient. This result aligns with previous studies on the impact of leading-edge tubercles on two-dimensional airfoils. However, earlier research on three-dimensional flipper models shows that leading-edge tubercles can enhance the maximum lift-to-drag ratio. This suggests that one of the functions of tubercles is to inhibit

the spanwise extension of tip vortices, offering improved control in three-dimensional flipper models.

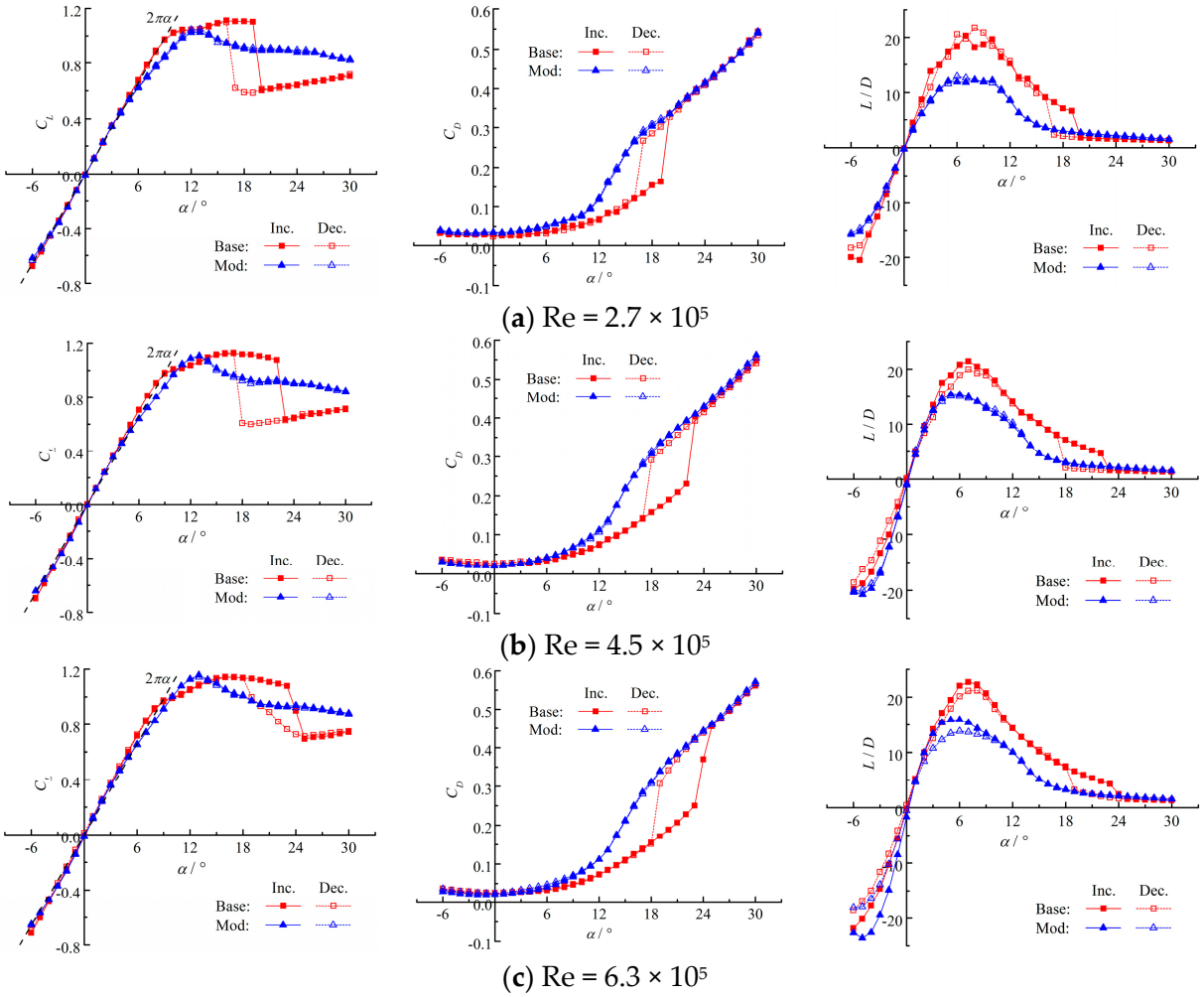
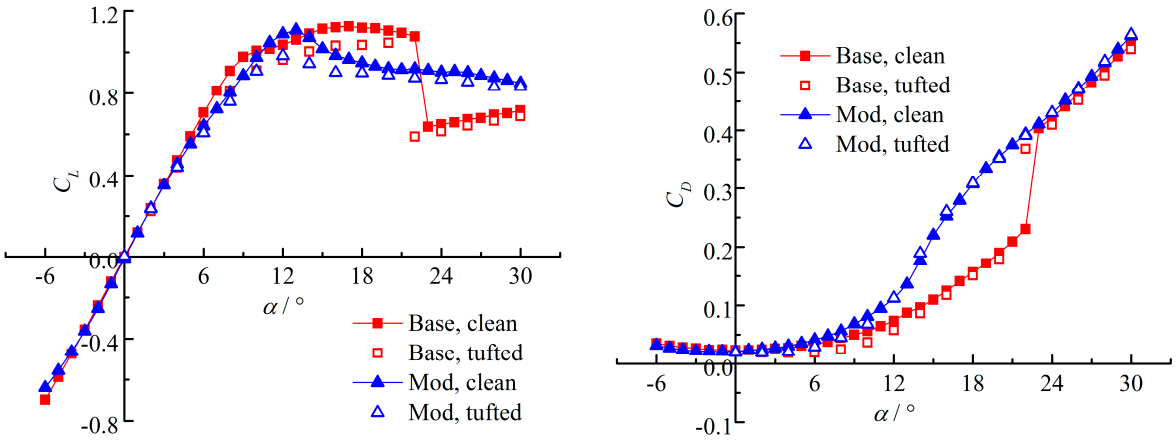


Figure 7. Comparison of the aerodynamic performance between the baseline and modified airfoils at different Reynolds numbers (left to right: lift coefficient, drag coefficient, lift-to-drag ratio).

3.2. Flow Visualization

3.2.1. Performance Verification

To assess the impact of tuft application on the aerodynamic performance of the test airfoils, force measurements were synchronized with the tuft visualization experiments. Figure 8 compares the aerodynamic performance of the clean and tufted airfoils during increasing AOA cases at Re = 4.5 × 10^5. Overall, the lift and drag coefficients of the tufted airfoils are similar to those of the clean airfoils. For both the baseline and modified airfoils, the lift coefficient is slightly lower at AOAs greater than 6°, likely due to the increased surface roughness. The stall angle of the baseline airfoil is reduced by about 1°, which may be attributed to the deep stall condition's sensitivity to environmental disturbances, given the strong hysteresis characteristics of the baseline airfoil. Nevertheless, the general trend of the performance curves is maintained for both airfoils. As a result, the tuft visualization is considered reliable in reflecting the flow patterns on the clean airfoils.

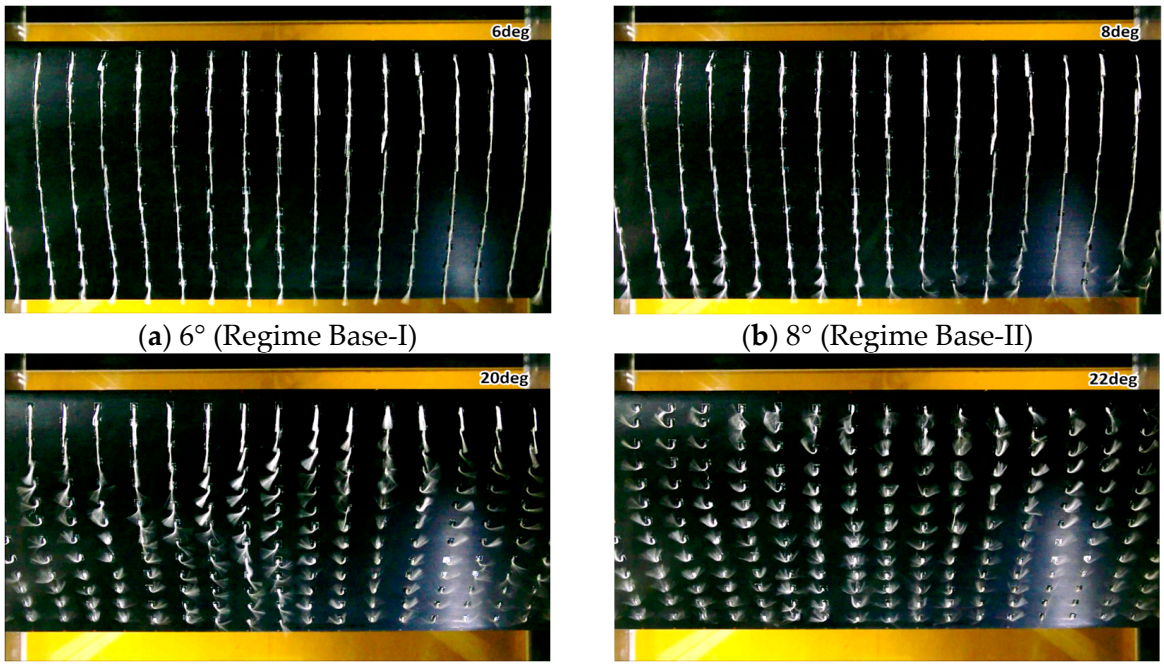


(**a**) Lift coefficient (**b**) Drag coefficient

Figure 8. Comparison of the aerodynamic performance between the clean and tufted airfoils (Re = 4.5 × 10^5, AOA increasing).

3.2.2. Flow Regimes on the Baseline Airfoil

Figure 9 presents the tuft visualization results of the baseline airfoil at selected AOAs for Re = 4.5 × 10^5. At 6° (Figure 9a), the flow remains fully attached to the suction surface, with all tufts steadily pointing downstream. As the AOA increases to 8° (Figure 9b), trailing-edge separation begins, indicated by the shaking motion of tufts near the trailing edge. With further increases in AOA, the trailing-edge separation vortex expands, and the separation line progressively moves toward the leading edge. Details on the development of this separation line can be found in our previous research [23]. Between 20° (Figure 9c) and 22° (Figure 9d), the flow undergoes an abrupt transition from trailing-edge to leading-edge separation, with all tufts on the suction surface shaking vigorously. For clarity, the conditions of full attachment, trailing-edge separation, and leading-edge separation are defined as Regimes Base-I, -II, and -III, respectively.



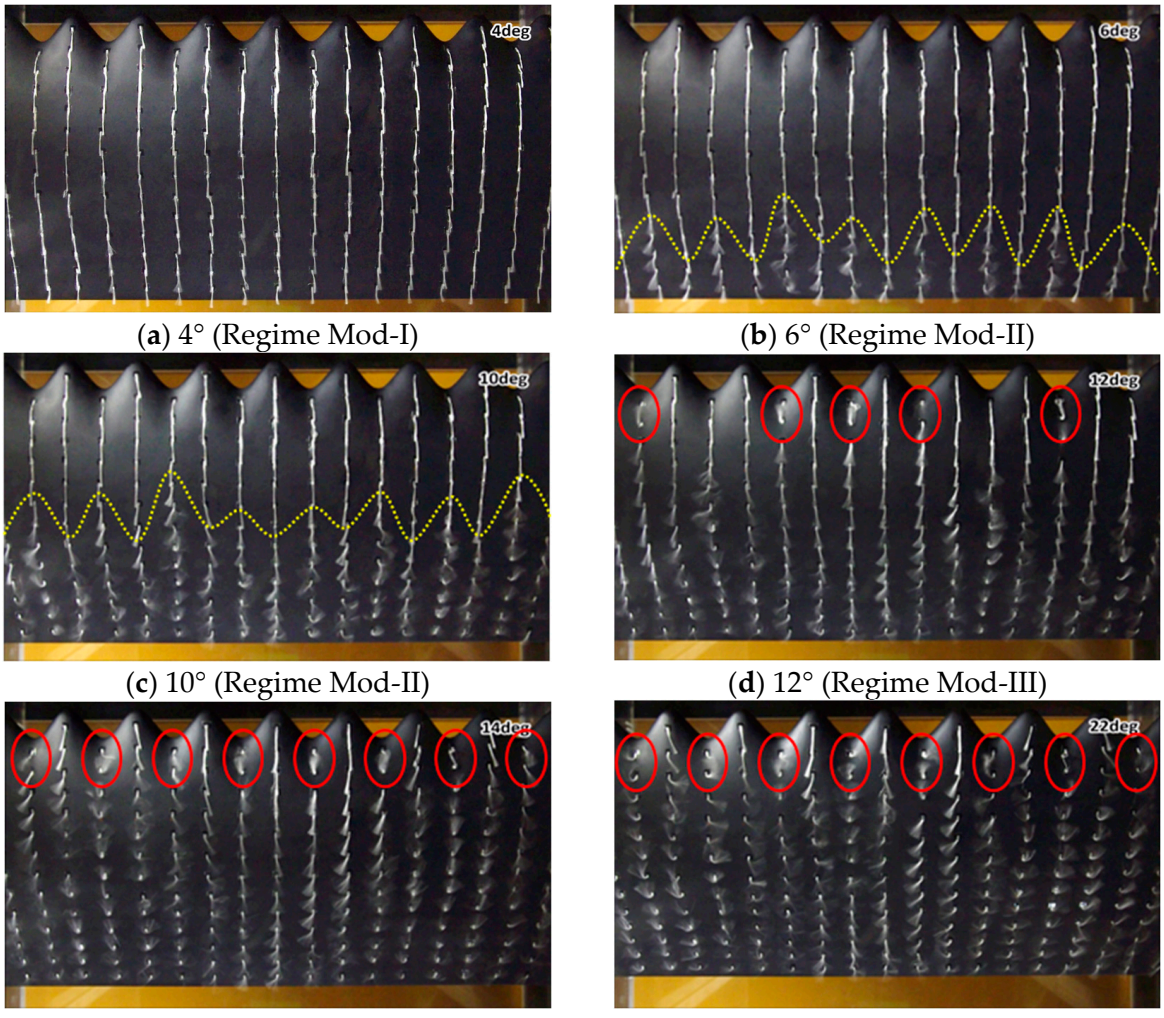
(**a**) 6° (Regime Base-I) (**b**) 8° (Regime Base-II)

(**c**) 20° (Regime Base-II) (**d**) 22° (Regime Base-III)

Figure 9. Tuft visualization result of the baseline airfoil (Re = 4.5 × 10^5, AOA increasing branch).

3.2.3. Flow Regimes on the Modified Airfoil

Figure 10 presents the tuft visualization results of the modified airfoil at the AOA increasing branch with a Reynolds number of 4.5×10^5. At an AOA of 4° (Figure 10a), the flow remains nearly fully attached, a state referred to as Regime Mod-I. As the AOA increases to between 6° and 10°, trailing-edge separation becomes evident, with more pronounced separation occurring along the valley sections, as shown by the wavy separation line in Figure 10b,c. This flow condition is classified as Regime Mod-II. At an AOA of 12° (Figure 10d), a new flow regime emerges, termed Regime Mod-III. In this regime, leading-edge separation is observed on some valley sections, where the first tuft near the leading edge exhibits strong, erratic motion, highlighted by red circles. For other valley sections not annotated, three to four tufts near the leading edge point stably downstream, indicating trailing-edge separation without leading-edge separation. On the peak sections, the flow remains attached for the distance of five tufts and points directly downstream, with no spanwise component. At AOAs of 14° and above (Figure 10e,f), all valley sections experience leading-edge separation. In this regime, spanwise interaction intensifies, resulting in a strong lateral component in the attached flow over the peak sections. This distinctive flow condition is classified as Regime Mod-IV.



(**a**) 4° (Regime Mod-I) (**b**) 6° (Regime Mod-II)

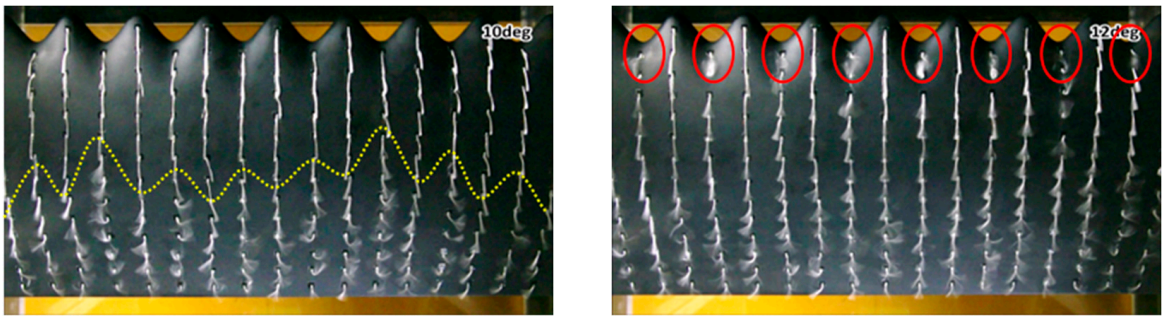
(**c**) 10° (Regime Mod-II) (**d**) 12° (Regime Mod-III)

(**e**) 14° (Regime Mod-IV) (**f**) 22° (Regime Mod-IV)

Figure 10. Tuft visualization of the modified airfoil at Re = 4.5×10^5 (yellow dot: approximate separation line; red circle: leading-edge separation on the local valley section).

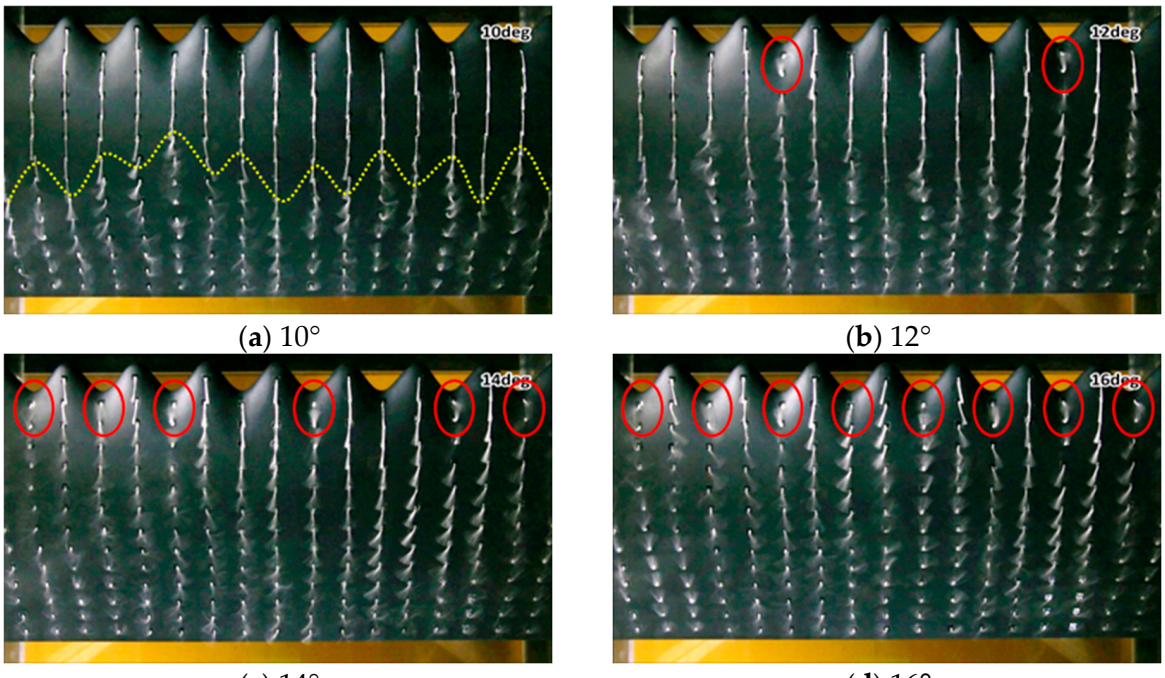
At different Reynolds numbers, the flow patterns remain generally similar, with the primary distinction being the transition process from Regime Mod-II to Mod-IV. At the

lower Reynolds number of 2.7 × 10^5 (Figure 11), the Mod-III regime is absent. At an AOA of 10° (Figure 11a), trailing-edge separation with a wavy separation line is observed, characteristic of the Mod-II regime. When the AOA increases to 12° (Figure 11b), leading-edge separation appears across all valley sections, which is a key feature of the Mod-IV regime. At the higher Reynolds number of 6.3 × 10^5 (Figure 12), the AOA range of the Mod-III regime expands. The flow condition at 10° (Figure 12a) is similar to that at the lower Reynolds number and falls within the Mod-II regime. At 12° (Figure 12b), the Mod-III regime is observed, with local leading-edge separation occurring on two valley sections within the viewing window. At 14° (Figure 12c), the number of valley sections experiencing local stall increases to six, though two valley sections remain in trailing-edge separation. When the AOA reaches 16° (Figure 12d), the Mod-IV regime is fully established, with leading-edge separation present on all valley sections.



(**a**) 10° (**b**) 12°

Figure 11. Transformation process from Regime Mod-II to Mod-IV at Re = 2.7 × 10^5 (yellow dot: approximate separation line; red circle: leading-edge separation on the local valley section).



(**a**) 10° (**b**) 12°

(**c**) 14° (**d**) 16°

Figure 12. Transformation process from Regime Mod-II to Mod-IV at Re = 6.3 × 10^5 (yellow dot: approximate separation line; red circle: leading-edge separation on the local valley section).

3.3. Judging Criterion of Different Flow Regimes

3.3.1. Criterion for the Baseline Airfoil

Based on the separation conditions observed in tuft visualizations, the AOA can be divided into distinct regions. According to the previous definition by Mccullough et al. [49], the stall type of the baseline airfoil across all tested Reynolds numbers is categorized as a combined trailing-edge and leading-edge stall. The segmented lift curve of the baseline airfoil is illustrated in Figure 13. Although Mccullough et al. [49] have thoroughly summarized these findings, they are presented here again for a clearer comparison with the modified airfoil in the next subsection. The AOA range is divided into three regions, i.e., Regimes Base-I, -II and -III. In the Base-I regime, the flow is fully attached, resulting in a linear increase in lift coefficient and relatively low drag. In the Base-II regime, the flow transitions to trailing-edge separation, causing the lift curve to deviate from linearity, forming a semi-rounded peak. Drag begins to increase at an accelerating rate. In the Base-III regime, leading-edge separation occurs, causing an abrupt drop in the lift curve, which then stabilizes at a lower level. Correspondingly, the drag curve shows a sudden increase followed by a relatively steady rise.

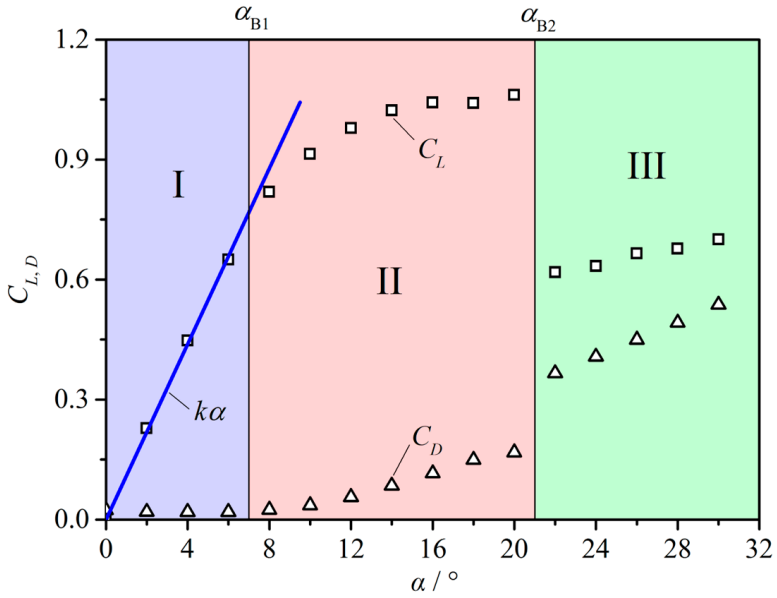


Figure 13. Lift and drag performance of the baseline airfoil corresponding to different flow regimes (I, II and III represent Regimes Base-I, II and III, respectively).

To provide a more quantitative analysis of the lift coefficient curve for the baseline airfoil, several characteristic parameters are defined and illustrated in Figure 13. The slope of the linear segment of the lift curve is denoted as k. The critical AOA between Regions B-I and B-II is defined as α_{B1}, while the critical AOA between Regions B-II and B-III is defined as α_{B2}. Additionally, the maximum lift coefficient $C_{L,\,max}$ is also selected as a key parameter for assessing the lift curve. The main parameters of the lift curve for the baseline airfoil at various Reynolds numbers are summarized in Table 1. It is observed that as the Reynolds number increases, α_{B1} tends to decrease, while α_{B2} tends to increase. The slope of the linear segment, which is slightly greater than the theoretical value of 2π, increases with the Reynolds number. Similarly, the maximum lift coefficient also shows an upward trend as Reynolds numbers increase.

Table 1. Characteristic parameters of the lift curve of the baseline airfoil.

Re	$k/2\pi$	α_{B1}	α_{B2}	$C_{L,\,max}$
2.7×10^5	1.030	8°	20°	1.1121

Table 1. *Cont.*

Re	$k/2\pi$	α_{B1}	α_{B2}	$C_{L,\,max}$
4.5×10^5	1.060	7°	23°	1.1254
6.3×10^5	1.083	7°	24°	1.1426

3.3.2. Criterion for the Modified Airfoil

As outlined in the introduction, there is currently no unified summary of the lift coefficient curve for airfoils with leading-edge tubercles. The primary goal of this research is to provide a comprehensive overview of the main characteristics of the lift curve for such modified airfoils. By synthesizing data from the lift and drag curves, as well as flow visualization, four distinct regimes are defined, as illustrated in Figure 14. In the Mod-I regime, the lift coefficient increases linearly at a rate close to the theoretical value, while the drag coefficient remains relatively low. This linear slope is defined as k_1. In this phase, the flow remains fully attached, as shown in the tuft visualization at 4° (Figure 10a). When the AOA exceeds the first critical AOA, α_{M1}, the lift curve deviates from the initial linear segment and begins to increase at a lower rate, denoted as k_2. At the same time, the drag coefficient starts to rise. In this region, a wavy separation line appears, with more pronounced separation in the valleys and reduced separation at the peaks, as depicted in the tuft visualizations in Figures 10b,c, 11a and 12a. Once the AOA surpasses the second critical AOA, α_{M2}, the lift curve deviates from the second linear segment and begins to decline with further increases in the AOA. The drag coefficient rises more significantly than in the Mod-II regime. Localized leading-edge separations occur in some tubercle valleys, as previously observed in the tuft visualizations in Figures 10d,e and 12b,c. As the AOA exceeds the third critical AOA, α_{M3}, the lift curve stabilizes after a further decline, while the drag coefficient increases in a pattern similar to the baseline airfoil at post-stall AOAs. In this region, leading-edge separation can be observed across all the valley sections, as shown in Figures 10e,f, 11b and 12d.

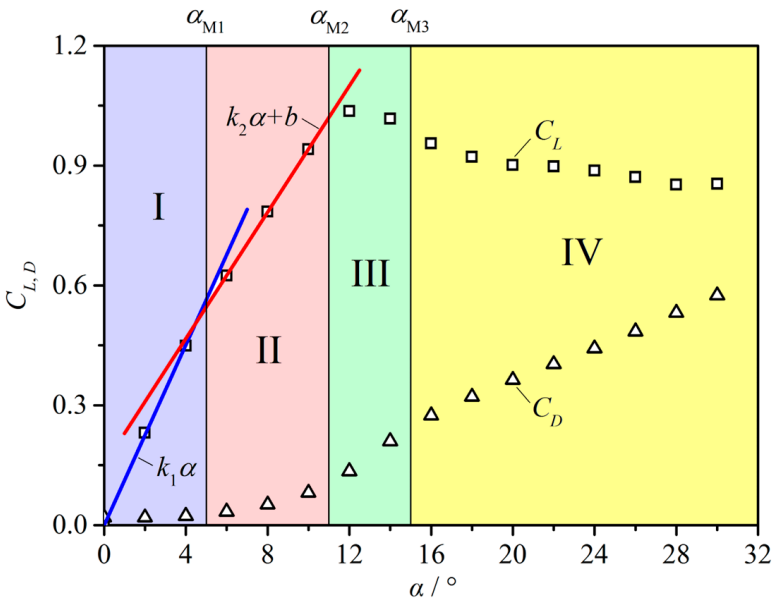


Figure 14. Lift and drag performance of the modified airfoil corresponding to different flow regimes (I, II, III, and IV represent Regimes Mod-I, II, III and IV, respectively).

The distribution of different flow regimes at different Reynolds numbers based on the tuft visualization results are shown in Figure 15, and the main parameters of the lift coefficient curve of the modified airfoil are summarized in Table 2. The critical AOAs are determined through a comprehensive assessment of the lift curve characteristics and tuft

visualizations, with values accurate to within 1°. It is observed that the value of $k_1/2\pi$ increases from 1.027 to 1.081 as the Reynolds number rises from 2.7×10^5 to 6.3×10^5, which are comparable to the lift slopes of the baseline airfoil. The first critical angle, α_{M1}, remains constant at 4° across different Reynolds numbers, which is lower than α_{B1} of the baseline airfoil, indicating an earlier onset of trailing-edge separation. The values of $k_2/2\pi$ range from 0.699 to 0.805 across the tested Reynolds numbers, leading to lower lift coefficients compared to the baseline airfoil. The second critical angle, α_{M2}, is consistently 11° across all Reynolds numbers, with the exception of the value at Re = 2.7×10^5, which is absent in Table 2 due to the lack of the Mod-III regime. The third critical angle, α_{M3}, increases from 11° to 15° as Reynolds numbers increase, likely due to the rise in flow momentum within the boundary layer as Reynolds numbers grow. Additionally, the maximum lift coefficient increases from 1.0264 to 1.1570 as the Reynolds number increases from 2.7×10^5 to 6.3×10^5.

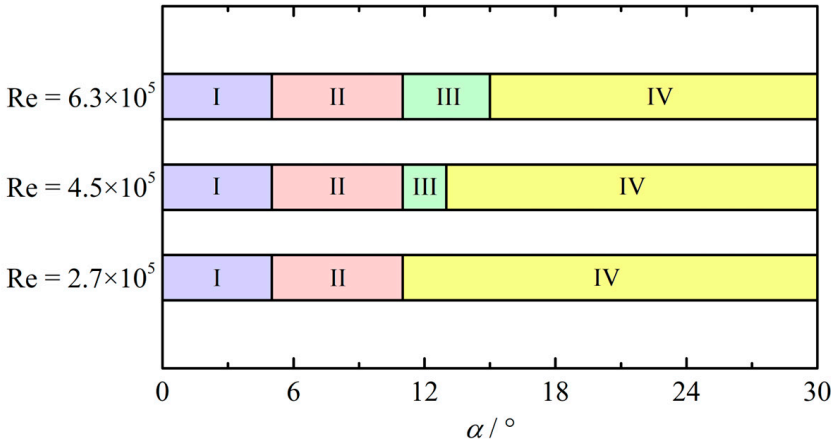


Figure 15. Distribution of different flow regimes at different Reynolds numbers based on tuft visualization result (I, II, III, and IV represent Regimes Mod-I, II, III and IV, respectively).

Table 2. Characteristic parameters of the lift curve of the modified airfoil.

$Re/10^5$	$k_1/2\pi$	α_{M1}	$k_2/2\pi$	α_{M2}	α_{M3}	$C_{L,\,max}$
2.7	1.027	5°	0.699	11°	11°	1.0264
4.5	1.064	5°	0.767	11°	13°	1.1076
6.3	1.081	5°	0.805	11°	15°	1.1570

3.4. Discussions

As summarized in the introduction, the normalization method for the lift and drag coefficients of a tubercled airfoil has not been standardized in previous research. Most studies use the average chord length to calculate these coefficients [17–20]. However, in some studies, including this one, which investigate the effect of protruding tubercles, the chord length of the valley section, equivalent to the baseline airfoil, has been used [22–25]. In a particular study by Stalnov et al. [26], sinusoidal leading edges were directly cut into the main body of the wing, and the lift coefficient was normalized using the baseline chord, mean chord, and valley chord, respectively. It was found that when the lift coefficient is defined based on the valley chord, uniformity in the lift curve slope can be achieved. This viewpoint is further validated in the present research. The modified airfoil in this study features extruded tubercles, resulting in a chord length larger than that of the baseline airfoil. However, when the lift coefficient is scaled by the valley section chord length, the lift slope values of the modified airfoil in Regime Mod-I closely match those of the baseline airfoil in Regime Base-I across different Reynolds numbers, as shown in Figure 7 and detailed in Tables 1 and 2. Thus, the valley section chord length is considered to be more appropriate to normalize the aerodynamic performance of a tubercled airfoil.

Regarding the flow control mechanism, this conclusion supports the previously proposed theory that tubercles act similarly to a series of small delta wings positioned along the leading edge, improving airfoil performance through vortex lift [32,42]. The counter-rotating streamwise vortices generated along the leading edges of the delta wings help maintain flow attachment over the wing, even as the angle of attack increases, delaying stall and enabling greater lift at steeper angles. The tuft visualization results in Figures 10–12 show that the tufts on all the peak sections remain attached, further supporting this mechanism. It can be considered that the delta wings are essentially installed in front of a straight-leading-edge wing in the airfoil shape of the valley section. Therefore, the valley section chord length is more suitable as the characteristic chord length for a modified airfoil with leading-edge tubercles. This conclusion is significant, as it can inform the optimal design of blades with leading-edge tubercles when applying this concept to wind turbines, tidal turbines, propellers, and other similar applications.

4. Concluding Remarks

In this paper, we investigate the effect of leading-edge tubercles on the aerodynamic performance and flow patterns of an airfoil through wind tunnel experiments, utilizing force measurements and tuft visualization at Reynolds numbers ranging from 2.7×10^5 to 6.3×10^5. A hysteresis loop is observed for the baseline airfoil near the stall angle, characterized by a sharp drop or recovery of the lift coefficient as the AOA increases or decreases. In comparison, the modified airfoil with leading-edge protuberances exhibits a smoother stall process and enhanced post-stall performance, though at the cost of reduced pre-stall performance.

Tuft visualization revealed four distinct flow regimes, corresponding to segments of the lift coefficient curve. In the first regime ($0^\circ \leq$ AOA $\leq 5^\circ$), the flow remained fully attached, with the lift coefficient increasing linearly at a slope similar to that of the baseline airfoil. In the second regime ($5^\circ \leq$ AOA $\leq 11^\circ$), trailing-edge separation occurred with a wavy separation line, causing the lift curve to deviate from its initial linear path and rise linearly at a lower slope. The first and second critical AOAs showed minimal variation with different Reynolds numbers. In the third regime, localized leading-edge separations appeared in some tubercle valleys, leading to a decline in the lift curve as the AOA increased further. In the fourth regime, leading-edge separation occurred across all valley sections, resulting in a nearly constant lift coefficient. The third critical AOA increased from 11° to 15° as the Reynolds number rose from 2.7×10^5 to 6.3×10^5, expanding the third regime.

Additionally, the study finds that normalizing the aerodynamic performance of a tubercled airfoil using the valley section chord length results in a lift slope in the first regime that closely matches that of the baseline airfoil across different Reynolds numbers. This method proves more appropriate than the traditional approach of using the averaged chord length. These results support the hypothesis that leading-edge tubercles function similarly to a series of delta wings along the airfoil's leading edge. The findings offer valuable insights and guidelines for optimizing the design of blades with leading-edge tubercles, with potential applications in wind turbines, tidal turbines, propellers, and similar technologies.

Author Contributions: Conceptualization, C.P.; Methodology, R.Z. and T.M.; Validation, X.F.; Formal analysis, K.M.; Investigation, P.L.; Data curation, J.K.; Writing—original draft, D.W. and C.C.; Supervision, Q.L. All authors have read and agreed to the published version of the manuscript.

Funding: This research was funded by the National Key R&D Program of China (No. 2022YFE0207000), the National Natural Science Foundation of China (No. 52206283), the high-tech industrialization special fund project of scientific and technological cooperation between Jilin Province and Chinese Academy of Sciences (No. 2023SYHZ0001), and the State Scholarship Fund of the China Scholarship Council (No. 202204910265).

Data Availability Statement: The original contributions presented in the study are included in the article, further inquiries can be directed to the corresponding author.

Conflicts of Interest: Authors Dian Wang and Rongyu Zha were employed by the company CRRC Qi Hang New Energy Technology Co., Ltd. Authors Chaoyi Peng, Xuebin Feng and Pengcheng Liang were employed by the company Zhuzhou Times New Materials Technology Co., Ltd. Author Jianyu Kou was employed by the company Inner Mongolia Energy Group Co., Ltd. The remaining authors declare that the research was conducted in the absence of any commercial or financial relationships that could be construed as a potential conflict of interest.

References

1. Aftab, S.M.A.; Razak, N.A.; Rafie, A.S.M.; Ahmad, K.A. Mimicking the humpback whale: An aerodynamic perspective. *Prog. Aerosp. Sci.* **2016**, *84*, 48–69. [CrossRef]
2. Bolzon, M.D.; Kelso, R.M.; Arjomandi, M. Tubercles and their applications. *J. Aerosp. Eng.* **2015**, *29*, 04015013. [CrossRef]
3. Fish, F.E.; Battle, J.M. Hydrodynamic design of the humpback whale flipper. *J. Morphol.* **1995**, *225*, 51–60. [CrossRef] [PubMed]
4. Fish, F.E.; Howle, L.E.; Murray, M.M. Hydrodynamic flow control in marine mammals. *Integr. Comp. Biol.* **2008**, *48*, 788–800. [CrossRef]
5. Fish, F.E.; Weber, P.W.; Murray, M.M.; Howle, L.E. The tubercles on humpback whales' flippers: Application of bio-inspired technology. *Integr. Comp. Biol.* **2011**, *51*, 203–213. [CrossRef]
6. Miklosovic, D.S.; Murray, M.M.; Howle, L.E.; Fish, F.E. Leading edge tubercles delay stall on humpback whale (*Megaptera novaeangliae*) flippers. *Phys. Fluids* **2004**, *16*, L39–L42. [CrossRef]
7. Downer, L.; Dockrill, P. *WhalePower Tubercle Blade Power Performance Test Report*; 61827278; Wind Energy Institute of Canada: Tignish, PE, Canada, 2008.
8. Zhang, R.K.; Wu, J.Z. Aerodynamic characteristics of wind turbine blades with a sinusoidal leading edge. *Wind Energy* **2012**, *15*, 407–424. [CrossRef]
9. Huang, C.C.; Bai, C.J.; Shiah, Y.C.; Chen, Y.J. Optimal design of protuberant blades for small variable-speed horizontal axis wind turbine-experiments and simulations. *Energy* **2016**, *115*, 1156–1167. [CrossRef]
10. Wang, Z.; Zhuang, M. Leading-edge serrations for performance improvement on a vertical-axis wind turbine at low tip-speed-ratios. *Appl. Energy* **2017**, *208*, 1184–1197. [CrossRef]
11. Shi, W.; Rosli, R.; Atlar, M.; Norman, R.; Yang, W. Hydrodynamic performance evaluation of a tidal turbine with leading-edge tubercles. *Ocean. Eng.* **2016**, *117*, 246–253. [CrossRef]
12. Shi, W.; Atlar, M.; Norman, R.; Aktas, B.; Turkmen, S. Numerical optimization and experimental validation for a tidal turbine blade with leading-edge tubercles. *Renew. Energy* **2016**, *96*, 42–55. [CrossRef]
13. Fan, M.; Sun, Z.; Yu, R.; Dong, X.; Li, Z.; Bai, Y. Effect of leading-edge tubercles on the hydrodynamic characteristics and wake development of tidal turbines. *J. Fluids Struct.* **2023**, *119*, 103873. [CrossRef]
14. Shi, W.; Atlar, M.; Norman, R. Detailed flow measurement of the field around tidal turbines with and without biomimetic leading-edge tubercles. *Renew. Energy* **2017**, *111*, 688–707. [CrossRef]
15. Butt, F.R.; Talha, T. Numerical investigation of the effect of leading-edge tubercles on propeller performance. *J. Aircr.* **2019**, *56*, 1014–1028. [CrossRef]
16. Asghar, A.; Perez, R.E.; Jansen, P.W.; Allan, W.D.E. Application of leading-edge tubercles to enhance propeller performance. *AIAA J.* **2020**, *58*, 4659–4671. [CrossRef]
17. Stark, C.; Shi, W.; Atlar, M. A numerical investigation into the influence of bio-inspired leading-edge tubercles on the hydrodynamic performance of a benchmark ducted propeller. *Ocean. Eng.* **2021**, *237*, 109593. [CrossRef]
18. Johari, H.; Henoch, C.W.; Custodio, D.; Levshin, A. Effects of leading-edge protuberances on airfoil performance. *AIAA J.* **2007**, *45*, 2634–2642. [CrossRef]
19. Hansen, K.L.; Kelso, R.M.; Dally, B.B. Performance variations of leading-edge tubercles for distinct airfoil profiles. *AIAA J.* **2011**, *49*, 185–194. [CrossRef]
20. Wei, Z.; New, T.H.; Cui, Y.D. An experimental study on flow separation control of hydrofoils with leading-edge tubercles at low Reynolds number. *Ocean Eng.* **2015**, *108*, 336–349. [CrossRef]
21. Serson, D.; Meneghini, J.R.; Sherwin, S.J. Direct numerical simulations of the flow around wings with spanwise waviness. *J. Fluid Mech.* **2017**, *826*, 714–731. [CrossRef]
22. Arai, H.; Doi, Y.; Nakashima, T.; Mutsuda, H. A study on stall delay by various wavy leading edges. *J. Aero Aqua Bio-Mech.* **2010**, *1*, 18–23. [CrossRef]
23. Cai, C.; Zuo, Z.; Morimoto, M.; Maeda, T.; Kamada, Y.; Liu, S. Two-step stall characteristic of an airfoil with a single leading-edge protuberance. *AIAA J.* **2017**, *56*, 64–77. [CrossRef]
24. Cai, C.; Zuo, Z.; Maeda, T.; Kamada, Y.; Li, Q.; Shimamoto, K.; Liu, S. Periodic and aperiodic flow patterns around an airfoil with leading-edge protuberances. *Phys. Fluids* **2017**, *29*, 115110. [CrossRef]
25. Gawad, A.F.A. Utilization of whale-inspired tubercles as a control technique to improve airfoil performance. *Trans. Control Mech. Syst.* **2013**, *2*, 212–218.
26. Stalnov, O.; Chong, T.P. Scaling of Lift Coefficient of an Airfoil with Leading-Edge Serrations. *AIAA J.* **2019**, *57*, 3615–3619. [CrossRef]

27. Sudhakar, S.; Karthikeyan, N.; Suriyanarayanan, P. Experimental studies on the effect of leading edge tubercles on laminar separation bubble. *AIAA J.* **2019**, *57*, 5197–5207. [CrossRef]
28. Wei, Z.; Zang, B.; New, T.H.; Cui, Y.D. A proper orthogonal decomposition study on the unsteady flow behaviour of a hydrofoil with leading-edge tubercles. *Ocean Eng.* **2016**, *121*, 356–368. [CrossRef]
29. Dropkin, A.; Custodio, D.; Henoch, C.W.; Johari, H. Computation of flow field around an airfoil with leading-edge protuberances. *J. Aircr.* **2012**, *49*, 1345–1355. [CrossRef]
30. Gross, A.; Fasel, H.F. Numerical investigation of passive separation control for an airfoil at low-Reynolds-number conditions. *AIAA J.* **2013**, *51*, 1553–1565. [CrossRef]
31. Cai, C.; Zuo, Z.; Liu, S.; Wu, Y. Numerical investigations of hydrodynamic performance of hydrofoils with leading-edge protuberances. *Adv. Mech. Eng.* **2015**, *7*, 1687814015592088. [CrossRef]
32. Custodio, D. The Effect of Humpback Whale-Like Leading Edge Protuberances on Hydrofoil Performance. Master Thesis, Worcester Polytechnic Institute, Worcester, MA, USA, 2007.
33. Hansen, K.L.; Rostamzadeh, N.; Kelso, R.M.; Dally, B.B. Evolution of the streamwise vortices generated between leading edge tubercles. *J. Fluid Mech.* **2016**, *788*, 730–766. [CrossRef]
34. Rostamzadeh, N.; Hansen, K.L.; Kelso, R.M.; Dally, B.B. The formation mechanism and impact of streamwise vortices on NACA 0021 airfoil's performance with undulating leading edge modification. *Phys. Fluids* **2014**, *26*, 107101. [CrossRef]
35. Zhao, M.; Zhang, M.M.; Xu, J.Z. Numerical simulation of flow characteristics behind the aerodynamic performances on an airfoil with leading edge protuberances. *Eng. Appl. Comput. Fluid Mech.* **2017**, *11*, 193–209. [CrossRef]
36. Rostamzadeh, N.; Kelso, R.M.; Dally, B. A numerical investigation into the effects of Reynolds number on the flow mechanism induced by a tubercled leading edge. *Theor. Comput. Fluid Dyn.* **2017**, *31*, 1–32. [CrossRef]
37. Zhao, M.; Zhao, Y.; Liu, Z.; Du, J. Proper orthogonal decomposition analysis of flow characteristics of an airfoil with leading edge protuberances. *AIAA J.* **2019**, *57*, 2710–2721. [CrossRef]
38. Pérez-Torró, R.; Kim, J.W. A large-eddy simulation on a deep-stalled aerofoil with a wavy leading edge. *J. Fluid Mech.* **2017**, *813*, 23–52. [CrossRef]
39. Seyhan, M.; Sarioglu, M.; Akansu, Y.E. Influence of Leading-Edge Tubercle with Amplitude Modulation on NACA 0015 Airfoil. *AIAA J.* **2021**, *59*, 3965–3978. [CrossRef]
40. van Nierop, E.A.; Alben, S.; Brenner, M.P. How bumps on whale flippers delay stall: An aerodynamic model. *Phys. Rev. Lett.* **2008**, *100*, 054502. [CrossRef]
41. Ni, Z.; Su, T.; Dhanak, M. An empirically-based model for the lift coefficients of twisted airfoils with leading-edge tubercles. *AIP Adv.* **2018**, *8*, 045123. [CrossRef]
42. Weber, P.W.; Howle, L.E.; Murray, M.M.; Miklosovic, D.S. Computational evaluation of the performance of lifting surfaces with leading-edge protuberances. *J. Aircr.* **2011**, *48*, 591–600. [CrossRef]
43. Watts, P.; Fish, F.E. The influence of passive, leading edge tubercles on wing performance. In Proceedings of the 12th International Symposium on Unmanned Untethered Submersible Technology, Durham, NH, USA, 27–29 August 2001.
44. Pedro, H.T.; Kobayashi, M.H. Numerical study of stall delay on humpback whale flippers. In Proceedings of the 46th AIAA Aerospace Sciences Meeting and Exhibit, Reno, NV, USA, 7–10 January 2008. AIAA 2008-584.
45. Cai, C.; Liu, S.; Zuo, Z.; Maeda, T.; Kamada, Y.; Li, Q.; Sato, R. Experimental and theoretical investigations on the effect of a single leading-edge protuberance on airfoil performance. *Phys. Fluids* **2019**, *31*, 027103. [CrossRef]
46. Cai, C.; Zhou, T.; Liu, S.; Zuo, Z.; Zhang, Y.; Li, Q. Modeling of the compartmentalization effect induced by leading-edge tubercles. *Phys. Fluids* **2022**, *34*, 087104. [CrossRef]
47. Rae, W.H.; Pope, A. *Low-Speed Wind Tunnel Testing*; John Wiley: Hoboken, NJ, USA, 1984.
48. AGARD (Advisory Group for Aerospace Research and Development). *Wind Tunnel Wall Corrections*; AGARD-AR-304; NATO Research and Technology Organization (RTO): Brussels, Belgium, 1994.
49. Mccullough, G.B.; Gault, D.E. *Examples of Three Representative Types of Airfoil-Section Stall at Low Speed*; NACA TN 2502; NASA: Washington, DC, USA, 1951.

Disclaimer/Publisher's Note: The statements, opinions and data contained in all publications are solely those of the individual author(s) and contributor(s) and not of MDPI and/or the editor(s). MDPI and/or the editor(s) disclaim responsibility for any injury to people or property resulting from any ideas, methods, instructions or products referred to in the content.